Early stages of InP nanostructure formation on AlInAs

Agnieszka M. Gocalinska,[1,*] Enrica E. Mura,[1] Marina Manganaro,[1,†] Gediminas Juska,[1] Valeria Dimastrodonato,[1] Kevin Thomas,[1] Andrew Zangwill,[2] Dimitri D. Vvedensky,[3] and Emanuele Pelucchi[1]

[1]*Tyndall National Institute, University College Cork, "Lee Maltings", Dyke Parade, Cork, Ireland*
[2]*School of Physics, Georgia Institute of Technology, Atlanta, Georgia 30332, USA*
[3]*Blackett Laboratory, Imperial College London, London SW7 2AZ, United Kingdom*

(Received 30 July 2019; revised manuscript received 16 March 2020; accepted 24 March 2020; published 27 April 2020)

The potential of $Al_xIn_{1-x}As$/InP as a flexible candidate for future device applications relies on a thorough understanding of the growth mechanisms of this system during metalorganic vapor-phase epitaxy (MOVPE). We present a systematic study of the morphology of InP films grown on macroscopically lattice-matched $Al_xIn_{1-x}As$ during low-pressure MOVPE. InP and AlInAs alloys are often assumed to be fully compatible, as long as macroscopic lattice matching is preserved. However, thin InP films show a variety of spontaneously formed nanostructures as the growth conditions are varied. We have examined the systematic variation of individual growth conditions (temperature, V/III ratios, growth rate, and misalignment angle and direction) to obtain a comprehensive picture of the morphological evolution of this system. The analysis of these experiments is based on a kinetic model of the deposition and decomposition of polyatomic precursors and the subsequent adatom kinetics, which is used to form characteristic lengths from combinations of kinetic coefficients associated with each process. The orderings of these lengths for particular ranges of growth conditions account for many aspects of the morphological evolution on perfectly oriented and misoriented surfaces. For perfectly oriented surfaces, differences in surface free energies are suggested as the driving force for Volmer-Weber growth and the observed formation of multilayer features. Finally, we examine the transition from quantum rings to quantum dots during postgrowth recovery when the group-V source is switched from phosphine to arsine. A qualitative explanation of similar observations in InAs/InP based on As/P exchange is consistent with our findings.

DOI: 10.1103/PhysRevB.101.165310

I. INTRODUCTION

The performance of modern semiconductor devices depends crucially on the integrity of the epitaxial growth process, i.e., control of the intrinsic impurity content, defect density of the bulk material, and critically, the compositional, structural, and morphological integrity of the interfaces. These characteristics and others must be taken into consideration, particularly for heterostructures, as even the best design can be detrimentally affected by unsuitable growth conditions or neglected structural issues, leading, for example, to broadened photoluminescence peaks or degraded electrical transport.

The III-V compounds InP and $Al_xIn_{1-x}As$ are broadly used and often grown together in multilayered structures for applications such as telecommunications. Indeed, the current drive toward complex photonic integrated circuits results in multilayer and multifunctional integration with InP-based photonic devices integrating several lasers, arrayed waveguide multiplexers and demultiplexers, modulators, polarization control stages, detectors, and various coupling devices on a single chip, requiring a multitude of III-V material combinations [1,2], including AlIn(Ga)As/InP heterostructure waveguides [3,4]. InP and $Al_xIn_{1-x}As$ also have an interesting type-II band alignment with a band gap in the one-micron range, making them suitable for conventional and advanced opto-microelectronics [5–7]. Their applications extend to more advanced devices with engineered band structures and typical quantum dot behavior, if a transition to type-I band alignment can be obtained [8].

Despite known issues with possible ternary alloy segregation and clustering [9–11] when grown by means of metalorganic vapor-phase epitaxy (MOVPE), $Al_xIn_{1-x}As$ and InP alloys are often assumed to be fully compatible, as long as macroscopic lattice matching is preserved [12,13]. However, we have previously reported [14] that, in the early nucleation stages of growth, InP grown on lattice-matched AlInAs develops three-dimensional (3D) nanostructures, instead of following simple layer-by-layer growth, indicating that the interface between InP and $Al_xIn_{1-x}As$ provides a challenging epitaxial scenario and the observed growth can be far from the expected Frank–van der Merwe mode [15–17]. Indeed, as our discussion suggests, this system fits more into the description of the Volmer-Weber growth mode [16–18], with multilayer island formation, most likely, with no wetting layer. This is somewhat surprising and rarely reported for conventional compound III-V materials, but is more widely seen in nitrides [19–21] and II-VI semiconductors [22]. Similar morphologies have also been observed [23–25] and simulated [26,27] in the metallic Co/Cu(001) system.

*Corresponding author: agnieszka.gocalinska@tyndall.ie
†Current address: Department of Physics, University of Rijeka, 51000 Rijeka, Croatia.

 ©2020 American Physical Society

During the early stages of epitaxy in the $Al_xIn_{1-x}As$/InP system, we have shown [28] that type-I band alignment can be obtained by enabling As/P exchange and creating InP(As) self-assembled nanostructures from the initial 3D growth of pure InP, allowing for emission at telecom wavelengths. Indeed, these newly discovered properties demonstrate the $Al_xIn_{1-x}As$/InP material system to be a flexible candidate for multiple device designs. In view of this, our observations of morphological evolution call for a thorough understanding of the growth mechanisms involved during precursor deposition, subsequent surface kinetic development, and postgrowth kinetics with various group-V precursors. The experiments and analysis we report here provide an important step in this direction.

In this paper, we report the results of a systematic study of the morphology of InP films and the resulting spontaneously formed nanostructures under a variety of growth conditions on a macroscopically lattice-matched $Al_xIn_{1-x}As$ buffer during MOVPE. We have examined the variation of each element of the growth conditions (temperature, V/III ratio, growth rate, and misalignment angle and direction) to understand their effect on the morphological evolution of the system, focusing on the initial stages of the process. This overview provides the information required to control the self-organized morphology, enabling the customized design of tailored devices with specified feature sizes and densities. The morphologies on perfectly oriented and misoriented surfaces are explained in terms of a model based on characteristic lengths obtained from a model that includes the main kinetic processes during MOVPE. The difference in the surface free energies of the two materials is suggested as the driving force for the Volmer-Weber growth mode and the observed multilayer features in experiments on perfectly oriented surfaces.

This paper is organized as follows. Our sample preparation, growth, and *ex situ* analysis are described in Sec. II. The kinetic model used to characterize growth modes is presented in Sec. III. This model is based on reaction-diffusion equations for the deposition and decomposition of polyatomic precursors and the subsequent adatom kinetics, with each process having a kinetic coefficient. Our analysis of the experiments is based on determining the characteristic length scales that determine the effectiveness of each process in determining the surface morphology. This approach sidesteps the uncertainties of determining the kinetic parameters by focusing on the expected morphology resulting from various orderings of these characteristic lengths. The characteristic lengths obtained from our model are worked out in the Appendix. The results of experiments obtained by systematically varying growth parameters (layer thickness, growth temperature, V/III ratio, and growth rate) are reported in Sec. IV. Our conclusions are provided in Sec. V. The Supplemental Material [29] shows additional line scans and images. Selected figures with different arrangements of the data are also shown, as well as several subsets of related samples, to provide additional insight into the systematics of our system.

II. METHODOLOGY

The samples used in the present study were grown by MOVPE at low pressure (80 mbar) in a commercial horizontal reactor with purified N_2 as the carrier gas. The precursors were trimethylindium (TMIn), trimethylaluminum (TMAl), trimethylgallium (TMGa), arsine (AsH_3), and phosphine (PH_3). The majority of the samples in this study consist of thin InP films of various thicknesses grown on $Al_{0.48}In_{0.52}As$ (hereafter referred to as AlInAs) layers of 100 nm thickness (unless stated otherwise) following 100 nm of homoepitaxial buffers on InP semi-insulating substrates. InP buffer growth conditions were optimized, as in Ref. [30].

Growth conditions for the AlInAs layer were fixed for the majority of the samples to a V/III ratio $R = 110$, a growth rate $G = 1\ \mu m/h$, and real estimated growth temperature $T_g = 600\,^{\circ}C$. The growth conditions for the nanostructured InP layers, $R = 180$, $G = 0.7\ \mu m/h$, $T_g = 630\,^{\circ}C$, were considered "standard" or the "starting point." However, for investigating the influence of growth conditions on the morphology, some of the parameters were varied over the ranges $R = 45$–430, $G = 0.12$–$1.4\ \mu m/h$, and $T_g = 530$–$665\,^{\circ}C$.

The choice of substrate offcut, which is known to have major effects in MOVPE [30–33], was limited to nominally perfectly oriented $(100) \pm 0.05^{\circ}$ wafers, and those slightly $(0.4^{\circ} \pm 0.05^{\circ})$ misoriented toward $[111]A$ or $[111]B$ planes, hereafter referred to as "p.o." (perfectly oriented), "$0.4^{\circ}A$" or "A," and "$0.4^{\circ}B$" or "B," respectively. In general, p.o. and misoriented samples were grown simultaneously (various substrates were loaded into the reactor in the same run), to reduce run-to-run reproducibility issues, which is particularly critical in the sensitive case of very thin layer growth. Subsets of different growth conditions are described in detail when the particular line of study is presented.

An additional subset of samples was grown with an $Al_xIn_{1-x-y}Ga_yAs$ layer instead of AlInAs to investigate critical Al concentrations. Several samples were grown with an additional 100 nm AlInAs layer on top of the InP nanostructures for photoluminescence studies. The growth conditions for the AlInAs cap were identical to those for the buffer layer; during the required temperature adjustment after InP deposition, the sample was kept under phosphine overflow.

Macroscopic lattice matching of the $Al_xIn_{1-x}As$ layers was confirmed by x-ray diffraction (XRD) with an X-Pert MRD diffractometer using a hybrid monochromator and a triple-axis analyzer. They reproducibly showed a composition of $x = 48\% \pm 0.5\%$. $Al_xIn_{1-x-y}Ga_yAs$ layers were occasionally slightly mismatched by design (they were dedicated for use in specific devices), though always fully pseudomorphic, and therefore maintaining the in-plane lattice parameter of the underlying InP. Their compositions were determined by a combination of XRD and photoluminescence (PL), and are indicated in the text were those samples are discussed.

Morphological studies were performed with a Veeco Multimode V atomic force microscope (AFM) in tapping/noncontact mode in air at room temperature. Samples were scanned perpendicular to the cleaving edge (zinc blende InP cleaves perpendicularly along [110] planes) across the main visible step flow. AFM images reported here show mainly the signal amplitude, which is clearer than height scans (therefore, no z scale is provided). Several height scans are shown for very flat surfaces to distinguish between individual crystallographic steps, or when this presentation is more informative.

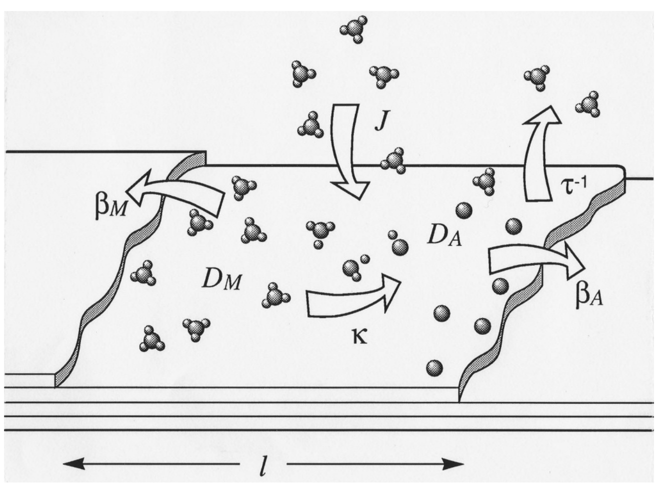

FIG. 1. Schematic depiction of the molecular and atomic kinetic processes included in the model defined by Eqs. (1)–(3).

The optical characterization was carried out in a conventional microphotoluminescence setup. The samples were cooled down to ∼10 K in a He closed-cycle cryostat. The excitation source was a laser diode emitting at 635 nm and operating in continuous-wave mode.

III. THE MODEL

The morphologies presented here will be analyzed in terms of a basic model for MOVPE in which the atomic constituents are delivered to the surface as polyatomic precursors. For III-V systems, this precursor contains the group-III species (TMIn, TMAl, and TMGa for the experiments reported here). Although the group-V species are not considered explicitly, their effect on the growth conditions can be included by varying the V/III ratio and determining the changes to the model parameters.

We consider the deposition onto a misoriented surface of a molecule that contains the atomic constituent of the growing substrate. In addition to deposition, the molecular surface kinetics included in our model are (i) desorption of molecules back into the gas phase, (ii) surface diffusion of molecules in a weakly bound precursor state, (iii) decomposition of molecules on a terrace to release the atomic constituent, and (iv) decomposition of the molecule at a step edge (Fig. 1). Also included are the atomic surface kinetics: (v) surface diffusion of the atomic species and (vi) incorporation of these atoms at a step edge. We ignore all site-blocking effects and the presence (and fate) of all molecular decomposition fragments. Desorption of the atomic species is also neglected.

Our reaction-diffusion equations generalize the analysis of Burton, Cabrera, and Frank [34] (BCF) to include the processes described above. The one-dimensional continuum BCF model has been used to analyze molecular-beam epitaxy (MBE) on misoriented surfaces [35]. In the present case, the evolutions in time and space of the surface concentrations of precursor molecules $n(x,t)$ and adatoms $c(x,t)$ are determined by the following coupled reaction-diffusion equations:

$$\begin{aligned}\frac{\partial n}{\partial t} &= D_M\frac{\partial^2 n}{\partial x^2} - \frac{n}{\tau} - \kappa n + J,\\ \frac{\partial c}{\partial t} &= D_A\frac{\partial^2 c}{\partial x^2} + \kappa n.\end{aligned} \tag{1}$$

Here, D_M and D_A respectively denote the surface diffusion constant of the precursor molecules and the adatoms, κ and τ^{-1} are the rate constants for decomposition and desorption of the precursor molecule on a terrace, and J is the molecular deposition flux. Equations (1) are supplemented by the boundary conditions at steps for the adatoms,

$$\begin{aligned}D_A c_x(0,t) &= \beta_A[c(0,t) - c_0],\\ -D_A c_x(\ell,t) &= \beta_A[c(\ell,t) - c_0],\end{aligned} \tag{2}$$

and the precursors,

$$\begin{aligned}D_M n_x(0,t) &= \beta_M n(0,t),\\ -D_M n_X(\ell,t) &= \beta_M n(\ell,t),\end{aligned} \tag{3}$$

where ℓ is the terrace length and c_0 is the equilibrium concentration of atoms at the step edge. As discussed elsewhere [35], the choice (2) indicates that adatoms incident on a step incorporate into the solid at a rate proportional to β_A. The choice (3) stipulates that every precursor molecule incident on a step decomposes at a rate proportional to β_M. In the steady state, the solutions to our equations have simple analytic forms [35] from which the growth rate can be determined. Although these equations can be generalized to two-dimensional surfaces, in the interest of obtaining a basic analytic theory, we will restrict ourselves to one-dimensional surfaces. This, of course, neglects any step meandering which, although an interesting phenomenon in its own right, does not play a significant role in the morphologies reported here.

Equations (1)–(3) have been used [30,31,36] to great effect to study the step-bunching instability during MOVPE on misoriented surfaces. For growth scenarios focusing on a *specific* feature, such as quantum dots formed in inverted pyramids, where many experiments can be repeated and kinetic parameters optimized, such models are capable of producing *quantitative* agreement with experimental measurements for their morphological and alloy concentration profiles over a range of growth rates and temperatures [37–39]. Our intention here, however, is not to parametrize the model (1)–(3) for the system at hand, but to use the kinetic parameters to identify characteristic lengths associated with the processes described by the model. This results in a basic analytic theory that can be used to understand systematically variations in surface morphology as the growth conditions are systematically varied. Table I summarizes the length scales obtained from the kinetic parameters in (1)–(3); further discussion about these parameters and their relation to growth modes is provided in the Appendix. As we discuss in Sec. V, our results provide the first step to a more detailed theory of InP growth modes on AlInAs.

IV. RESULTS AND DISCUSSION

In Ref. [14], we have briefly shown how the initial deposition of monolayers (MLs) of InP on AlInAs layers proceeds

TABLE I. The length scales obtained from the kinetic parameters in (1)–(3), together with their physical meaning. When two lengths are compared the shorter length corresponds to the faster process.

Length	Definition	Description
ℓ	miscut and orientation	terrace length
x_s	$\sqrt{D_M \tau}$	distance a molecule diffuses before desorbing
ℓ_κ	$\sqrt{D_M/\kappa}$	distance a molecule diffuses before decomposition (to release an adatom)
ℓ_A	$\sqrt{D_A/J_{\mathrm{eff}}}$	distance an adatom diffuses before another adatom is released by decomposition
ℓ_M	$\sqrt{D_M/J}$	distance a molecule diffuses before encountering another deposited molecule
d_A	D_A/β_A	additional distance an adatom diffuses (after first arrival at a step) before incorporation
d_M	D_M/β_M	distance a precursor diffuses before step-catalyzed decomposition and incorporation

on perfectly oriented substrates and on substrates with small misorientations. We discussed the variety of observed features with respect to specific growth conditions and substrate type, revealing a surprising degree of organization at the nanoscale. Here, we provide a much more in-depth analysis and more wide-ranging discussion encompassing a greater variety of morphologies resulting from a broader range of growth conditions and substrates. We interpret many of our results in terms of length scales in Table II. We then briefly summarize photoluminescence properties and conclude by discussing the implications of our results for possible device growth and future directions for optoelectronic applications.

Before presenting our results, we point out that densities quoted for various feature sizes should be treated only as observational estimates. In particular, determining the features to associate with fully or partially formed quantum dots or rings is not always straightforward, with inherent uncertainties and accompanying error bars. These densities were determined mainly for p.o. wafers as, in many cases, the background surface organization of misoriented wafers was too complicated. We stress that even "perfectly oriented" wafers have a certain tolerance of the offcut, resulting in $\lesssim 0.05^\circ$ deviation from the (001) crystallographic plane, without control of the type of steps exposed [group-III-terminated $(111)A$ or group-V-terminated $(111)B$]. Because of the extreme sensitivity of the resulting morphology to the precise misorientation, we anticipate variations in samples grown on wafers coming from different substrate batches. Therefore, we do not treat feature densities as "hard data," but instead focus on the qualitative trends and phenomenology.

The data presented in this section are separated into growth, growth interruption, and photoluminescence. In Sec. IV A the influence of the growth conditions during InP nanostructure layer formation on the final morphology is discussed with respect to each variable studied: layer thickness, growth temperature, V/III ratio, and growth rate. Section IV B focuses on the Al(Ga)InAs buffer layer. Section IV C shows the effect of hydrides during growth interruption on the resulting InP nanostructuring. The photoluminescence properties of capped samples are discussed in Sec. IV D.

A. InP growth conditions

1. Layer thickness

Figure 2 shows an overview of how epitaxial layers develop on differently misoriented substrates from the "starting point" growth conditions (refer to Figs. 1 and 2 of the Supplemental Material [29] for a different image arrangement). The

TABLE II. The hierarchy of regimes corresponding to the relative magnitudes of the characteristic lengths emerging from the coefficients in (1)–(3). The Appendix provides the definitions of these lengths and a discussion of their physical significance. For each regime, the predominant diffusing species, their terrace population, the kinetics at steps, and the resulting surface morphology are indicated.

Diffusing species	Terrace population	Step permeability	Surface morphology
$\ell_\kappa \ll x_s$ (atoms)	$\ell_A \ll \ell$ (high)		islands
	$\ell_A \gg \ell$ (low)	$d_A \ll \ell$ (impermeable)	fast atomic step flow
		$d_A \gg \ell$ (permeable)	slow atomic step flow
$\ell_\kappa \gg x_s$ (molecules)	$\ell_M \ll \ell$ (high)		molecular interactions (liquid-like state, collisional decomposition, ...)
	$\ell_M \gg \ell$ (low)	$d_M \ll x_s$ (impermeable)	fast molecular step flow
		$d_M \gg x_s$ $\ell_\kappa \ll d_M$	atomic kinetics (clusters or step flow)
		$d_M \gg x_s$ $\ell_\kappa \ll d_M$ (permeable)	slow molecular step flow

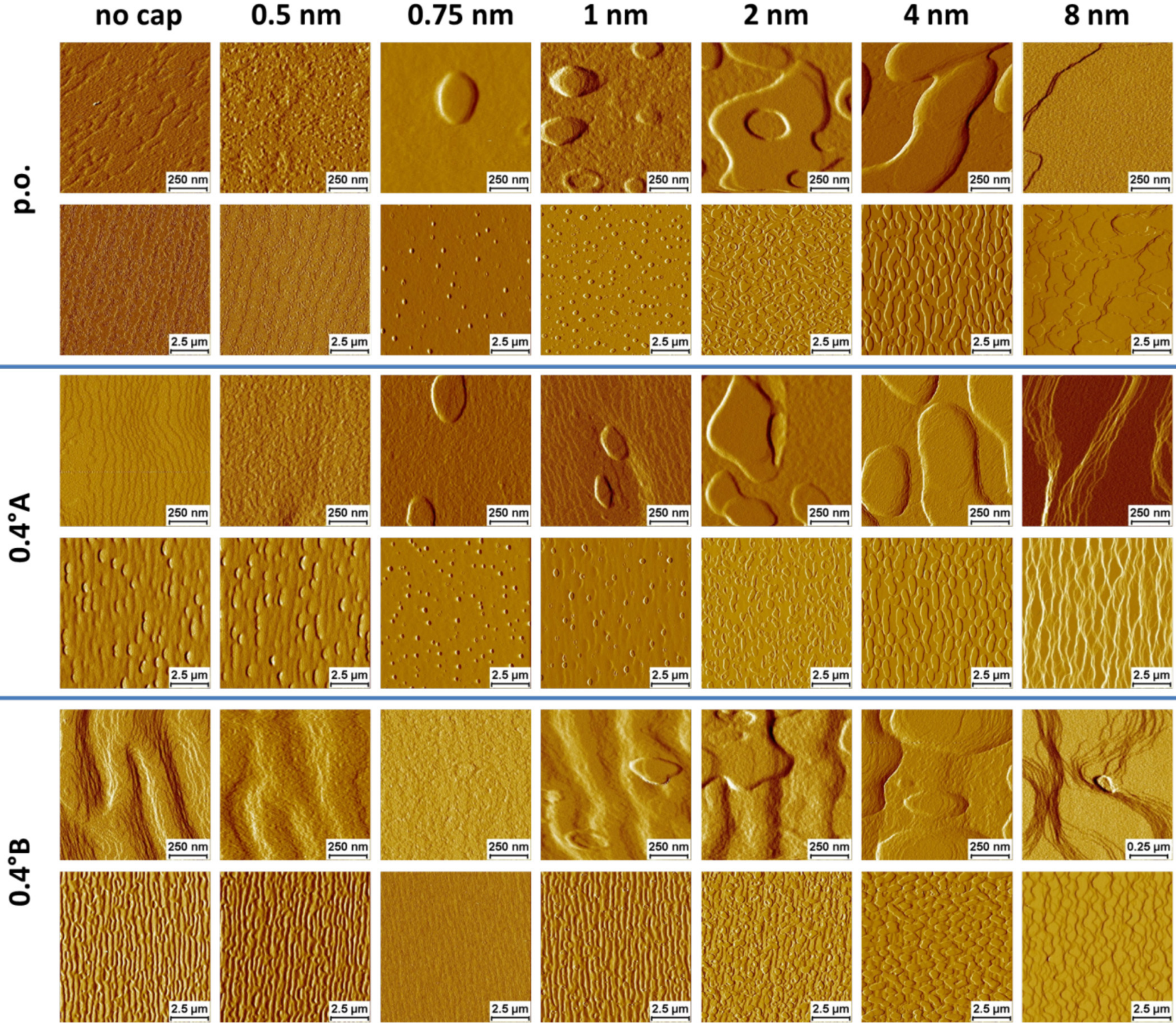

FIG. 2. Surface morphologies (AFM signal amplitudes) of representative samples grown at 630 °C, $G = 0.7$ μm/h, $R = 180$. The columns correspond to different InP cap layer thicknesses. The row pairs show respective images for differently misoriented substrates in two X-Y scales: 1×1 μm^2 (upper rows) and 10×10 μm^2 (lower rows).

underlying AlInAs has its own distinct morphologies on the miscut wafers (Fig. 2, column labeled "no cap"), showing step flow and step bunching, which is partially preserved during the early stages of InP overgrowth. Layers on the p.o. and 0.4°A wafers start to show nanostructuring of InP as soon as ∼3 MLs are deposited (0.75 nm), forming features of various height, but, interestingly, not exceeding 8 nm. A mixture of dots and rings is observed, whose densities and lateral sizes increase as more material is deposited. After a nominal deposition of 8 nm of a uniform planar layer of InP, organization is complete and appears with a surface organization similar to those reported for the same misorientations in the case of planar InP homoepitaxy [28]. For the 0.4°B wafer, the evolution is somewhat different. Nucleation appears to be delayed, as for a 0.75 nm InP layer thickness, and we observe only a small number of rings. Moreover, the layer is not fully planarized after 8 nm of InP growth, despite showing strong step bunching. Holes are visible, and in the scan presented in Fig. 3, have depth of 8 nm, while clearly showing the morphology of the underlying AlInAs. There is likely no InP present inside, i.e., no wetting layer.

Referring to Table II, as ℓ is the largest length scale for p.o. surfaces, there is a high density of diffusing species, which leads to the formation of islands in the early stages of growth. For the misoriented surfaces, where precursor decomposition occurs primarily at step edges ($\ell_\kappa \gg x_s$), growth would be expected to occur by step flow, as indeed is observed for the B surface, though not for the A surface. We can understand this by noting that the (111)B steps of III-V semiconductors are generally more reactive than (111)A because of the larger density of dangling bonds due to unshared electron pairs [40]. Hence, once a group-III species attaches to such a step edge, either through migration or a decomposition reaction, subsequent detachment is less likely than from a

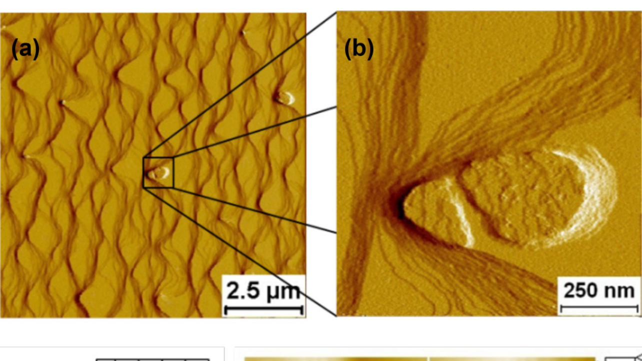

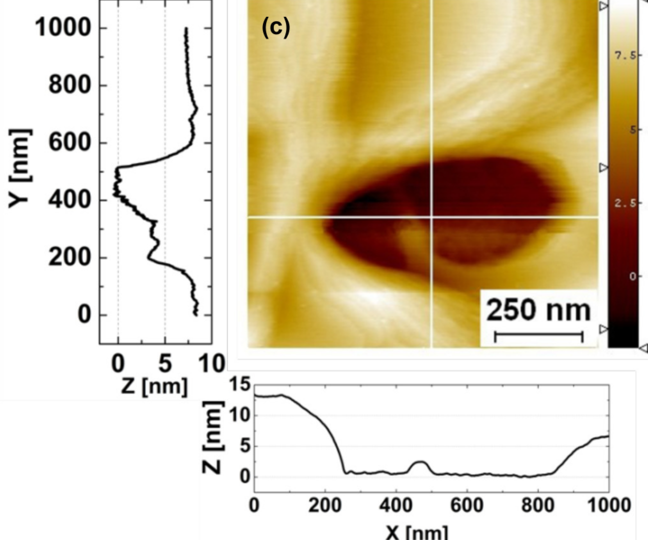

FIG. 3. Surface morphology of a representative sample grown at 630 °C, $G = 0.7$ μm/h, $R = 180$ on B the substrate with nominally 8 nm thick InP layer (direct regrowth of sample shown in Fig. 2). Images (a) and (b) show signal amplitudes; image (c) shows signal height in the zoomed-in image with corresponding X and Y profiles [41]. Remarkably, inside the hole, the underlying AlInAs organization seems preserved.

group-III-terminated (A) step. This has the effect of reducing the group-V adatom or fragment concentration on the terraces, therefore, suppressing island nucleation and promoting step flow. These are the trends seen up to 1 nm deposition in Fig. 2 for the three types of surfaces. The differences between the A and B steps could be taken into account by orientation-dependent coefficients in the boundary conditions (2) and (3).

When the nominal InP layer thickness reaches 2 nm we observe the direction in which the islands were growing and coalescing. For the A-type wafer, the elongation occurred in the same direction as the organization of steps on the underlying AlInAs, while, for B-type wafers, the nanostructures grew across the visible step organization (particularly evident in Fig. 2, in the columns labeled "4 nm," "0.4°A," and "0.4°B" in 10×10 μm^2 scale); i.e., the islands seem to be always aligned along the same crystallographic direction, irrespective of the original (small) substrate miscut.

However, the observation of the formation of the nanostructures on nominally perfectly oriented surfaces was sometimes not fully reproducible at a specific nominal deposition. Direct regrowth of the recipe previously resulting in distinct nanostructures on wafers from different batches occasionally resulted in a flat surface, very similar to those observed for thinner layers. As mentioned above and evident in Fig. 2 (the column labeled "0.75 nm"), the formation of the dots on the B-type surface is somewhat delayed with respect to the required minimal thickness, so we attribute the lack of full reproducibility of the "borderline thickness" samples to a variation of the slight misorientation of the perfectly oriented wafers to unintentionally exposing B-type steps (and, possibly, to run-to-run layer thickness variations, as we cannot precisely control the layer thickness to less than 0.3 MLs with the growth rate we used).

As a further note, the use of a surfactant during growth [trimethylantimony (TMSb)] [42] resulted in the modification of the top morphology. InP(Sb) seemed more "keen" to wet the AlInAs buffer, resulting in less distinct nanostructures, especially in the case of the B-type surface (Fig. 4 of the Supplemental Material [29]).

2. Growth temperature

Flattened images, surface images, and line scans obtained from atomic force microscopy (AFM) of lattice-matched AlInAs surfaces after the deposition of a 1 nm InP cap at $G = 0.7$ μm/h with $R = 180$ and $T_g = 530$ °C, 565 °C, 600 °C, 630 °C, and 665 °C are shown in Fig. 4. InP has the zinc blende structure with a lattice constant of 5.87 Å = 0.587 nm, so the deposition of 1 nm corresponds to about 3.5 (In-P) bilayers of InP.

The flattened and surface images of growth at 530 °C reveal a discernible step structure, but with highly disordered terraces. The line scans show regular fluctuations in the range of ~4 nm, which are presumably bunched steps [31]. The flattened images for growth at 565 °C show many small anisotropic islands and several holes, the latter particularly evident in the surface and line scans. The line scans indicate that most of these small islands have heights of ~1.2 nm, corresponding to approximately 4 In-P bilayers (Fig. 3, and Fig. 3 of the Supplemental Material [29]).

The images for growth at 600 °C show a smaller density of mostly isotropic islands and the appearance of rings. The islands have a more uniform lateral size compared to those grown at 565 °C. The line scans indicate that these islands have heights in the range 2.2–3.5 nm, which are close to integer multiples of the lattice constant of InP. The heights of the islands appear to have a broader range of values than those grown at 565 °C.

Growth at 630 °C continues the trend observed for growth at 565 °C and 600 °C. There are fewer islands, which are fairly isotropic, and there are many more rings. The islands are more regularly spaced, have a more uniform lateral size distribution, but a broader vertical distribution than those at lower temperatures. The line scans indicate that the largest islands have heights of ~6 nm, while the smallest are ~2 nm in height. The rings have smaller lateral sizes than the islands and there are islands that appear to be in various stages of ring formation. This indicates that the rings form from the islands. The mechanism for ring formation will be discussed later.

Finally, the images for growth at 665 °C show the simultaneous presence of steps and islands on terraces. With 4

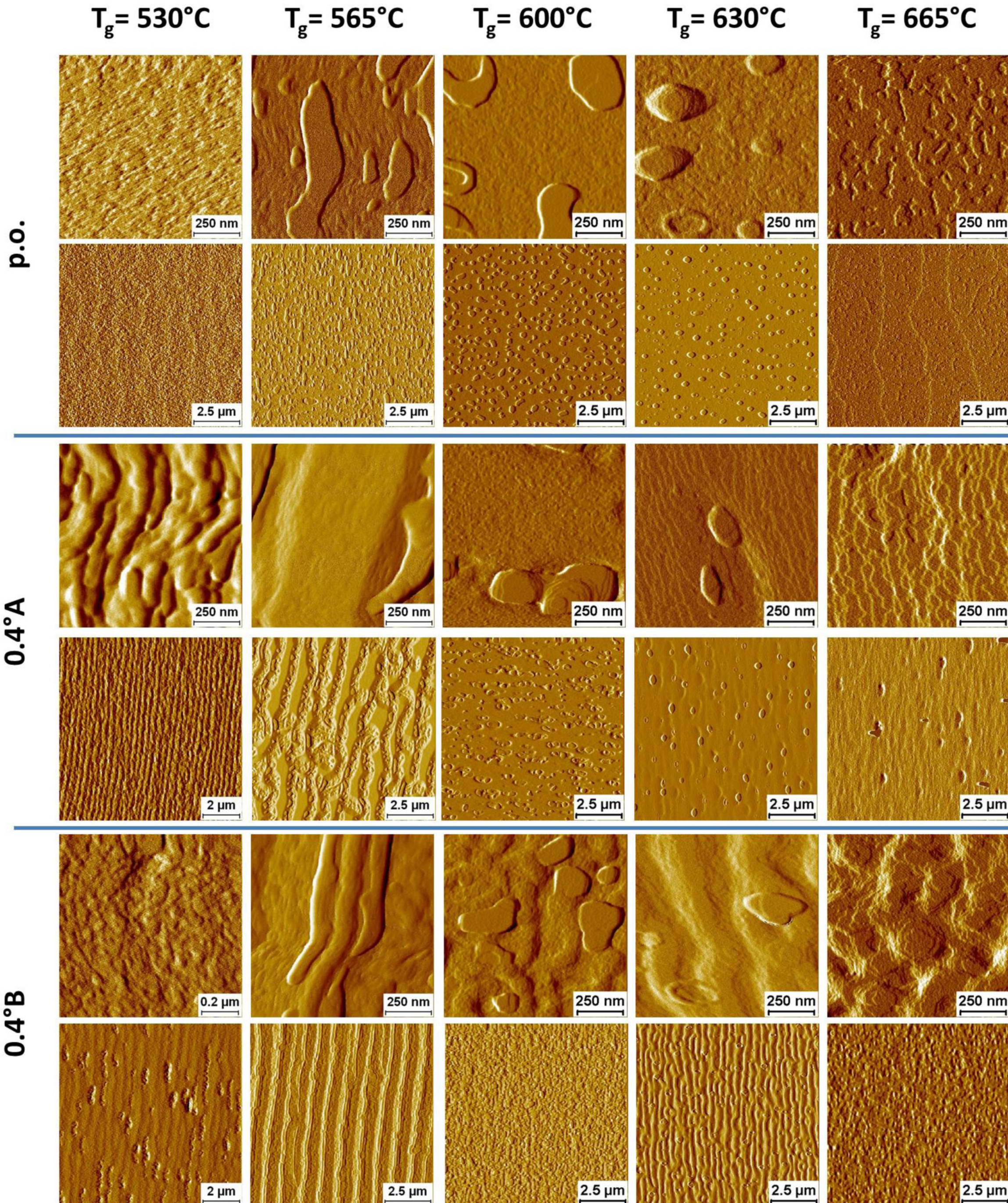

FIG. 4. Surface morphologies (AFM signal amplitudes) of representative samples grown with 1 nm InP cap at $G = 0.7\ \mu\text{m/h}$, $R = 180$. The columns correspond to different InP cap layer growth temperatures. The row pairs show respective images for differently misoriented substrates in two X-Y scales: $1 \times 1\ \mu\text{m}^2$ (upper rows) and $10 \times 10\ \mu\text{m}^2$ (lower rows). (See Fig. 3 of the Supplemental Material [29] for alternative data arrangement and line scans.)

terraces within the 10 μm scan range, the average terrace length is $\sim$2.5 μm. The line scan also indicates that the height difference across the steps is $\sim$2 nm. As there are 4 steps in this scan, the height of each step corresponds to a lattice constant, i.e., two In-P bilayers. Note the appreciable meandering of the steps.

The growth morphologies at 565 °C, 600 °C, and 630 °C appear to be the most indicative of growth on perfectly oriented surfaces, as steps play no role in the growth kinetics. The basic scenario seems to be based on fairly rapid decomposition of TMIn, after which the morphology is determined by the In migration kinetics. At 565 °C, a migrating indium atom is more likely to encounter another such atom, rather than an island, resulting in many small islands with a fairly uniform height distribution. As the temperature increases, the balance of these encounters gradually changes in favor of island growth, yields fewer islands, but with a broader height distribution. The increased temperature also seems to favor

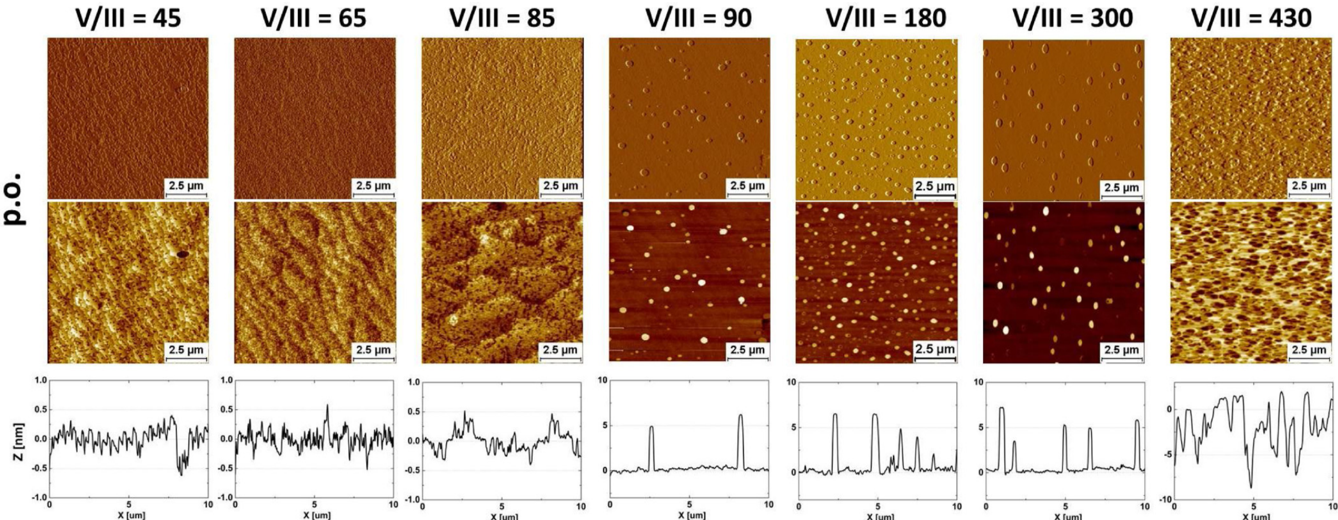

FIG. 5. Representative surface morphologies [AFM signal amplitudes (top row), heights (middle row), and height profiles (bottom row)] of samples grown on a nominally perfectly oriented (p.o.) substrate at 630 °C and $G = 0.7\ \mu\text{m/h}$ with a 1 nm InP cap, with different V/III ratios.

the formation of rings, as their density increases substantially from 600 °C to 630 °C.

The analysis of the morphologies of the misoriented surfaces in Fig. 4 begins with the observation, noted earlier, that the group-V-terminated steps (*B* type) are more reactive than the group-III-terminated steps (*A* type). This has been demonstrated by surface-diffraction measurements during homoepitaxy on misoriented GaAs(001) surfaces [43], where the incorporation barrier was found to be three times greater at *A*-type than at *B*-type surfaces. While this scenario serves as a qualitative guide for the present study, a more specific analysis which clarifies the trends in Fig. 4 by assessing the importance of the various processes in terms of their relative characteristic length scale is carried out in the Appendix.

The general trend we expect is that molecular processes (diffusion and decomposition at step edges) dominate at low temperatures, while atomic processes (onset of precursor decomposition on terraces, atomic diffusion, attachment/detachment at steps) gradually become active with increasing temperature. At 530 °C, the *A* surface shows a series of steps which reflect the original misorientation. The surface at 565 °C shows a step-bunching instability, but with a disordered array of the bunched steps. This corresponds to the transition from slow to fast molecular step flow (Table II). At the lower temperature, several attempts (at different steps) are needed for the step-catalyzed decomposition reaction to release an In atom. The temperature is too low for this atom to detach from the step, which results in step flow. The step train is still unstable with respect to step bunching, but the low temperature delays the onset of the instability. Similar trends are seen for the *B* surface, but with a more developed step-bunching instability with an ordered train of bunched steps due to the lower barrier to incorporation and the concomitant rapid transition from step flow. At the higher temperatures, there is a further transition to slow molecular step flow, with some island formation on the terraces, followed by fast step flow, where incorporation is rapid. The *B* surface shows the step train more clearly, while the *A* surface shows island formation more clearly. At the highest temperature (665 °C), a disordered step array is clearly discernible on the *A* surface, while the *B* surface shows scant evidence of the original misorientation. This could be due to adatom detachment after the relatively facile decomposition reaction at the steps.

3. V/III ratio

Figure 5 shows the impact of the V/III ratio used to grow the InP layer on the resulting nanostructuring. To highlight the changes, we show the results obtained on perfectly oriented substrates, as the background surface organization of AlInAs does not obscure or complicate the image interpretation. The decomposition of the precursor can occur either at a step edge (steps are present even on nominally perfectly oriented surfaces) or on the terrace. In the former case, steps play an important role in catalyzing the reaction, while the latter requires a sufficient group-III flux. Although increasing the V/III ratio increases the adatom population on the terraces, the increasing group-V flux decreases the mobility of these adatoms. Referring to Table II, decreasing the mobility of precursors and adatoms decreases ℓ_M and ℓ_A, respectively, eventually entering the regime where $\ell_A \ll \ell$ and $\ell_M \ll \ell$. The result is a window of V/III flux where dots and rings form, whose density increases, then decreases, and disappears altogether for higher V/III ratios. For extremely high V/III ratios, the layer closes, showing more of a "network" morphology than individual multilayered islands. The highest (individual) feature density is observed for $R = 180$ and is reduced for both higher and lower values of V/III (Table III). The feature type changes, with almost no rings observed for $R = 90$, but with comparable numbers of dots and rings for $R = 180$ and $R = 300$. The change in the aspect ratio of the nanostructures (the slight elongation at $R = 300$) could again be attributed to substrate misorientations and not necessarily to the high V/III ratio.

The height of the features in each case did not exceed 8–10 nm, as observed previously for all other growth conditions.

TABLE III. Densities (10^8 cm^{-2}) of rings and dots obtained from the AFM images in Fig. 5 for the indicated V/III ratios at 630 °C and $G = 0.7$ μm/h, with a 1 nm InP cap.

V/III	90		180		300	
Feature	dots	rings	dots	rings	dots	rings
Density	0.5	0.03	1.9	1.2	0.45	0.45

For $R = 430$, with what we could call a "quasiporous" surface, the peak-to-peak height values were inside that range as well. We were also able to identify some imperfections in the low-R layers, showing holes inside which the underlying AlInAs morphology was observed (Fig. 5, the column labeled $R = 45$). The depth of those holes roughly corresponds to the nominal layer thickness deposition (~0.7 nm).

Also noteworthy is that the transition between step flow and island formation is abrupt: for $R = 85$ we observe a "normal" InP morphology, while for $R = 90$, the nanostructuring is already evident. The layer appearance does not significantly change with reduced R. The fact that the more "traditional" surface organization is observed for lower R is actually quite surprising, in view of what we have shown in Ref. [28], where the high R was found to be a crucial requirement for high quality and uniform InP layer growth.

To discriminate between the influence of R and the amount of phosphine flowing through the reactor during growth, we performed several tests by keeping a fixed phosphine flux while changing R and, therefore, changing the growth rate. The results pointed toward R, not the net amount of PH_3 present during growth. However, we have also found that the growth rate itself has an influence on the surface morphology, so these results are not fully independent (and are not shown here).

4. Growth rate

Figure 6 shows how the morphology changes with increasing growth rate of InP (again on a 1 nm InP cap). The perfectly oriented and A surfaces show islands whose density increases with growth rate. For the perfectly oriented surface, the key characteristic length is ℓ_A (Table I), which decreases with increasing growth rate, i.e., with incoming TMGa flux and, therefore, increasing J_{eff} (Appendix). This produces the same effect on morphology as decreasing the temperature, namely, an increase in the density of islands. In fact, in the analysis of island densities for homoepitaxial growth of two-dimensional islands [44] and heteroepitaxial growth of three-dimensional islands [45], ℓ_A emerges as the appropriate scaling variable. Table IV quantifies the increased feature density on the perfectly oriented surface with increased growth rate. A similar trend is observed on the A surface, though at the lowest growth rates, the greater incorporation rates at steps lead to step bunching.

The B surfaces are, once again, slightly slower to reveal dot formation, as below 0.48 μm/h they are not observed, either due to the growth mechanism, or because they are hard to distinguish from the (rough) background morphology. Because of the lower barrier to adatom incorporation, steps and steps bunching dominate the morphology. In fact, this trend is also seen in the molecular-beam (MBE) of homoepitaxial GaAs(001)-(2×4) [43], where the more facile adatom incorporation rate on B surfaces and the concomitant reduction in the adatom density on the terraces results in the persistence of step flow to higher temperatures than on the A surfaces.

B. AlInAs buffer growth conditions

1. V/III ratio, temperature, and doping

We have investigated several growth temperatures for depositing the AlInAs layer, as well as the V/III ratio and the effect of carbon bromine doping. None of these had any qualitative impact on the nanostructuring of the overgrowth with InP with all samples consistently showing rings and dots. Apart from slightly different background surface morphologies, especially on the misoriented wafers and more organized step formation at higher temperatures, the other observed differences were not significant enough to warrant any conclusions and could be assigned to wafer-to-wafer misorientation variations and run-to-run reproducibility (Fig. 5 of the Supplemental Material [29]).

2. Thickness

In Fig. 7 we show how the nanostructuring of InP depends on the thickness of the underlying AlInAs buffer (here on perfectly oriented substrates), highlighting the role of interface reactivity. Even with only a fraction of a monolayer present, the subsequent InP overgrowth is not proceeding uniformly. When full AlInAs coverage is well established (0.5 nm, 2 InP MLs), distinct InP nanostructuring is formed. No rings are observed for thin AlInAs films, which is the only qualitative difference from the overgrowth on a bulk AlInAs layer.

We can account for this behavior from thermodynamic wetting arguments based on interfacial free energies [16]. We denote the free energy of the epilayer/vacuum interface by γ_e, that of the epilayer/substrate interface by γ_i, and that of the substrate/vacuum interface by γ_s. The Frank–van der Merwe (layer-by-layer) growth mode is favored if

$$\gamma_e + \gamma_i < \gamma_s. \tag{4}$$

In this case, as the epilayers are formed, the free energy *decreases* initially before attaining a steady-state value for

TABLE IV. Densities (10^8 cm^{-2}) of rings and dots obtained from the AFM images on the perfectly oriented surfaces in Fig. 6 for the indicated growth rates at 630 °C and $R = 180$, with a 1 nm InP cap.

	0.24 μm/h		0.36 μm/h		0.42 μm/h		0.7 μm/h		1.42 μm/h	
Feature	dots	rings	dots	rings	dots	rings	dots	rings	dots	rings
Density	0.9		6		0.8	0.5	1.9	1.2	2	1.5

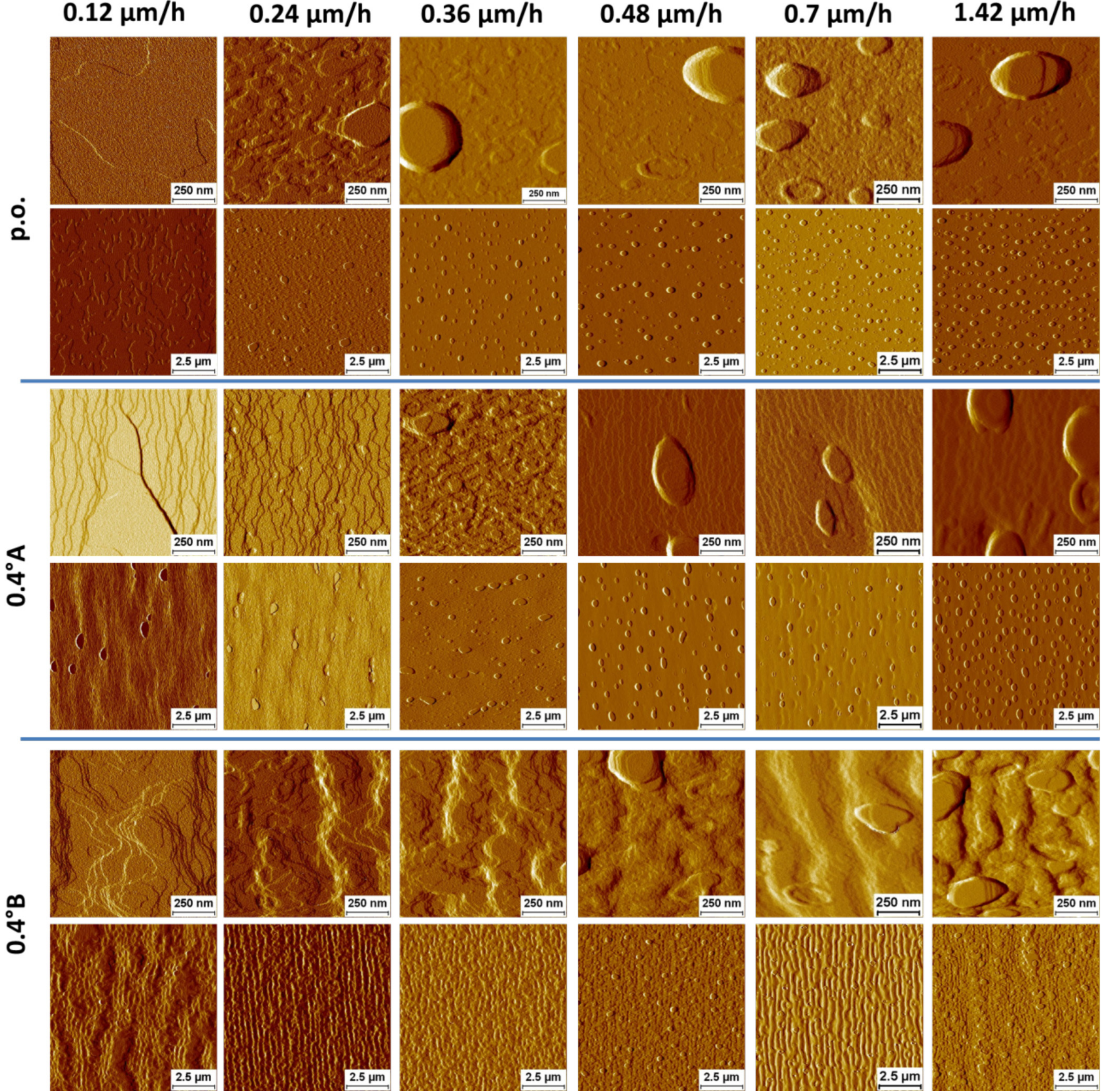

FIG. 6. Surface morphologies (AFM signal amplitudes) of representative samples grown with a 1 nm InP cap at 630 °C with $R = 180$. The columns correspond to different InP cap layer growth rate. The row pairs show respective images for differently misoriented substrates on two X-Y scales: 1×1 μm^2 (upper rows) and 10×10 μm^2 (lower rows).

thicker films. Alternatively, Volmer-Weber growth is favored if

$$\gamma_e + \gamma_i > \gamma_s, \tag{5}$$

in which case the free energy *increases* if epilayers are formed on the substrate, rendering a uniform layer thermodynamically unstable against a break-up into regions where the substrate is covered and those where it is uncovered. The morphological changes in Fig. 7 with increasing buffer layer thickness are consistent with a transition from close to layer-by-layer growth (for 0.125 nm AlInAs) to the appearance of well-developed three-dimensional islands (for 2 nm AlInAs).

Figure 7 illustrates the interplay between kinetics and thermodynamics in the morphological evolution with different surface free energies caused by varying the buffer layer thickness. As the substrates are nominally perfectly oriented, the average terrace length dominates over all other length scales (Table I). The interisland separation for the two thickest buffer layers is large enough to suggest that molecular, rather than atomic, diffusion provides the length scale for the initial island density. Island density is determined both by kinetic (critical

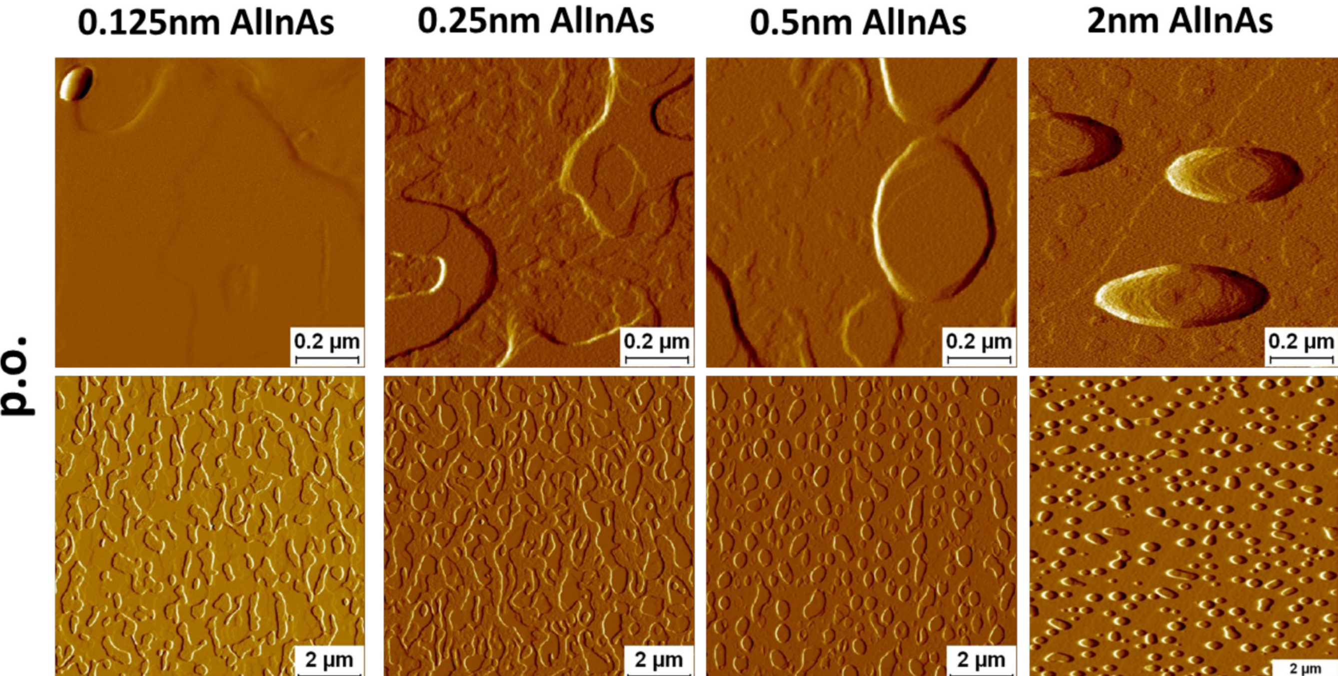

FIG. 7. Representative surface morphologies (AFM signal amplitudes) of 1 nm InP deposited on perfectly oriented substrate at 630 °C, $G = 0.7$ μm/h, $R = 180$ following AlInAs buffer of various thicknesses. The rows show images on two X-Y scales: 1×1 μm^2 (upper row) and 10×10 μm^2 (lower row).

island size, which in turn, depends on the deposition rate and substrate temperature) and thermodynamic factors (binding energies within the island and to the substrate, which reflect any differences in surface free energies) [46]. The sequence of morphologies in Fig. 7 provides a striking example of the influence of thermodynamics, as the fundamental kinetic parameters in Table I are unaltered. With increasing buffer layer thickness, which causes γ_i to increase, the morphological evolution changes from the nucleation, growth, and coalescence of two-dimensional islands for the thinnest buffer layer, to the gradual change to the nucleation and growth of three-dimensional (coherent) islands. Taken together, this sequence provides a striking illustration of the transition between the inequalities in (4) and (5).

The important point about the morphologies in Fig. 7 is that, when depositing InP on lattice-matched bulk InGaAs, we have never observed InP nanostructure formation; i.e., an InGaAs layer suppresses the InP nanostructuring. An extreme example is shown in Fig. 8(a), where a 1 nm InP layer was grown on top of a single monolayer of InGaAs on top of bulk AlInAs. The step formation is as expected, following a normal surface reconstruction. However, with an increasing concentration of Al in the $Al_xIn_{1-x-y}Ga_yAs$ alloy, we observe a deviation from this mechanism as early as for >10% Al. The sample shown in Fig. 8(b) (with 10% Al) already is less smooth. The aggregation is not yet evident, but in Fig. 8(c) (17% Al) the layer is clearly not uniform. As soon as the alloy composition reached 35% [Fig. 8(d)], the nanostructuring become obvious, with distinctive, separate multilayer islands.

C. Gas-switching sequence

In the device structure experiment, from which this study originated, there was a requirement for growth interruption between AlInAs and InP layers and, for consistency, this was kept for the duration of the study presented here. To explore this aspect further, we have investigated the influence that growth interruption and the gas-switching sequence have on InP nanostructure formation. The "starting conditions" led to a mixture of dots and rings on the AlInAs surface [Fig. 9(a)]. Introducing a 5-second phosphine preflow (i.e., the AlInAs layer was exposed to phosphine and arsine for 5 seconds before InP deposition; the gases were injected at the same fluxes as during the respective layer deposition) did not significantly affect the feature density and still preserved the mixed formation [Fig. 9(b)]. Removing arsine entirely from the reactor chamber by providing only PH_3 directly before InP deposition for 5 seconds led to a drastic reduction in ring density, while nearly only dots remained [Fig. 9(c)]. Eliminating the growth interruption and changing abruptly from AsH_3 to PH_3 led to much higher aspect ratio and size diversity, with again the full elimination of the rings [Fig. 9(d)]. The densities of dots and rings are compiled in Table V.

These observations are in line with those of our previous study of how postgrowth hydrides affect InP morphology in terms of the densities of dots and rings [28]. That study found that nanostructures exposed to phosphine, arsine, or

TABLE V. Densities (10^8 cm^{-2}) of rings and dots obtained from the AFM images in Fig. 9 for the indicated growth interruption conditions in panels (a)–(d) at 630 °C, $R = 180$, and $G = 0.7$ μm/h.

	Fig. 9(a)		Fig. 9(b)		Fig. 9(c)		Fig. 9(d)	
Feature	dots	rings	dots	rings	dots	rings	dots	rings
Density	0.9	1.2	1.2	0.9	1.5	0.03	6	

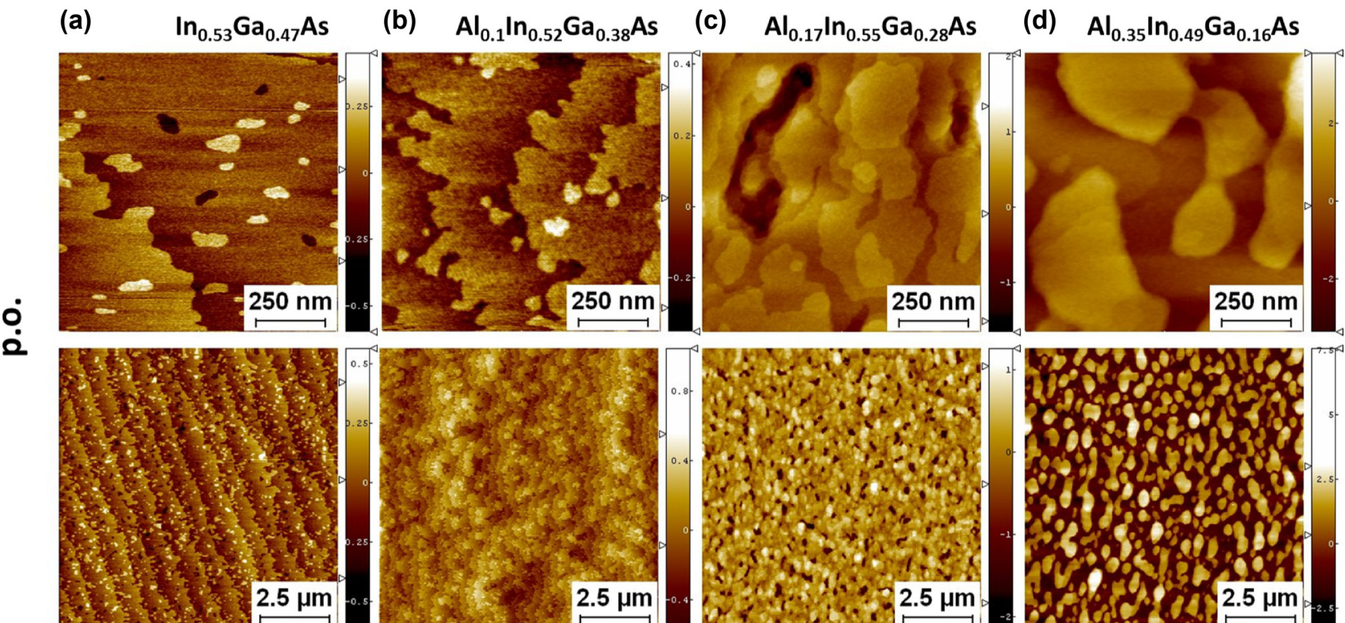

FIG. 8. Representative surface morphologies (AFM signal height, Z in nm) of thin InP layer deposited on perfectly oriented (p.o.) substrate at 630 °C, G = 0.7 μm/h, $R = 180$ following AlInGaAs buffer of various compositions. Sample structures: (a) 100 nm AlInAs/1 ML InGaAs/1 nm InP; (b), (c), and (d) 100 nm $Al_xIn_{1-x-y}Ga_yAs$/2 nm InP. The rows show images on two X-Y scales: 1×1 μm^2 (upper row) and 10×10 μm^2 (lower row).

a sequence of both showed a significant variation in morphology, especially in the transformation of dots into rings. We proposed that the composition of the nanostructures was altered by As incorporation into InP, a conclusion supported by photoluminescence measurements, with a clear type-I to type-II transition after the appropriate hydride exposure and capping protocol was implemented (this effect was also noticed, though to a lesser extent, in the capped structures in Ref. [47]). In our study [28], wet chemical etching also pointed to a noticeable incorporation of arsenic atoms into the InP layer, particularly in the centers of the nanostructures. The fact that the arsine overflow during growth interruption before InP deposition results in a higher ring density, while pure phosphine, or no growth interruption at all, brings a

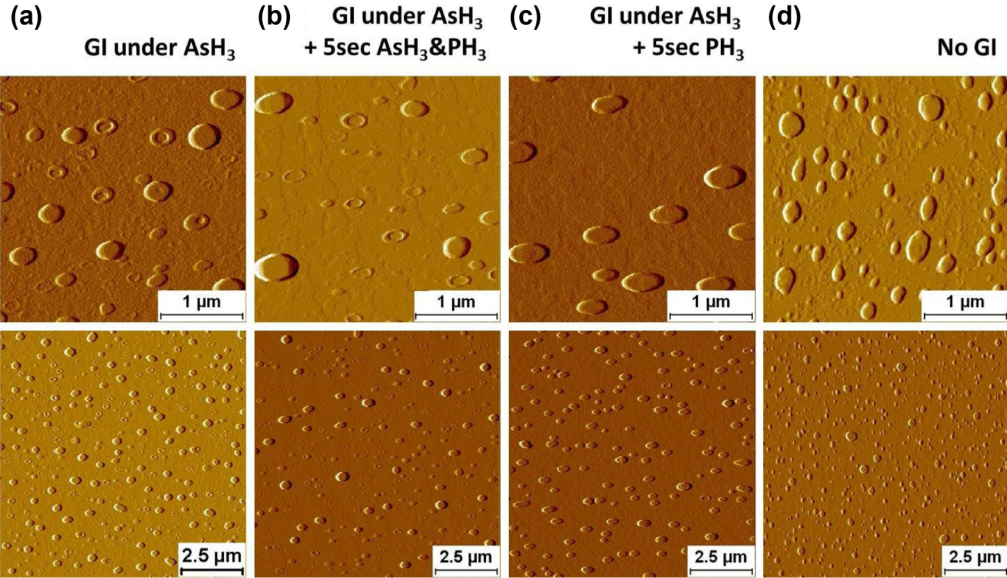

FIG. 9. Representative surface morphologies (AFM signal amplitudes) of 1 nm InP deposited on p.o. substrate at 630 °C, $G = 0.7$ μm/h, $R = 180$ on AlInAs after different growth interruptions, as indicated in the figure. The rows show images on two X-Y scales: 1×1 μm^2 (upper row) and 10×10 μm^2 (lower row). [Note that the "no GI" sample was grown on AlInAs deposited at 630 °C (same temperature as InP deposition), while all the other samples were grown on AlInAs deposited at 600 °C.]

more dotlike morphology, correlates well with those previous observations.

Similar conclusions were drawn for the postgrowth switching of the group-V precursor of InAs/InP, which also showed the transformation of quantum dots to quantum rings [48]. In particular, the transformation of dots to rings was seen in the postgrowth morphological evolution with a tertiarybutylphosphine source. The authors noted a significant temperature dependence in the rate of this transformation, with a change from 560 °C to 540 °C producing a significant decrease in the rate of the process. A model was proposed for the dot-to-ring transformation based on As/P exchange and the subsequent migration of the released In atoms from the top of the dots to the base of their sides. This exchange mechanism suggests that the rings have an appreciable incorporation of P atoms, but no evidence was provided, and the model was qualitative, with no supporting calculations.

Theoretical [49] and simulation [50] studies have addressed more controlled growth scenarios than the reactive environment of MOVPE. The formation of rings during droplet epitaxy of GaAs, as imaged in real time with *in situ* surface electron microscopy, revealed some similar morphologies to those in Ref. [28]. Thus, the theoretical model used in Ref. [49] may, with suitable modifications to account for the difference growth conditions, help to explain the kinetics of quantum ring formation during postgrowth switching of the group-V source.

D. Photoluminescence

Several of the previously discussed sample structures were selected for photoluminescence study. To provide sufficient confinement, the samples were capped with a 100 nm AlInAs layer. The top cap morphology was not ideal, clearly indicating the presence of a disturbed and not planarized interface below [e.g., Fig. 10(a)]. In Fig. 10(b) we present representative (low temperature) spectra of such structures. Photoluminescence is compared to a reference sample containing bulk AlInAs grown on an InP substrate made with the same growth conditions. It can be seen that when InP dots/rings are present, there are additional type-II-like peaks observed, and that their position and intensity are strongly dependent on the exact growth conditions of the nanostructured layer.

We point out again that, very likely, the features observed on the surface of uncapped samples and what is preserved inside the AlInAs matrix after capping are not morphologically identical, as, e.g., Ostwald ripening and other mobility-related processes are expected to occur during the cool-down of uncapped samples (and, probably in this case, some interface reactivity, as discussed above). Nevertheless, the observed photoluminescence indicates that the nanostructures are already developing at the epitaxial growth stage and do not form solely during cool-down, a relevant fact for clarifying phenomenology of their formation. This is especially valuable in MOVPE, where very little information can be gathered *in situ*. The cross-sectional transmission electron microscopy measurements done on a similar capped structure [47] also support that observation.

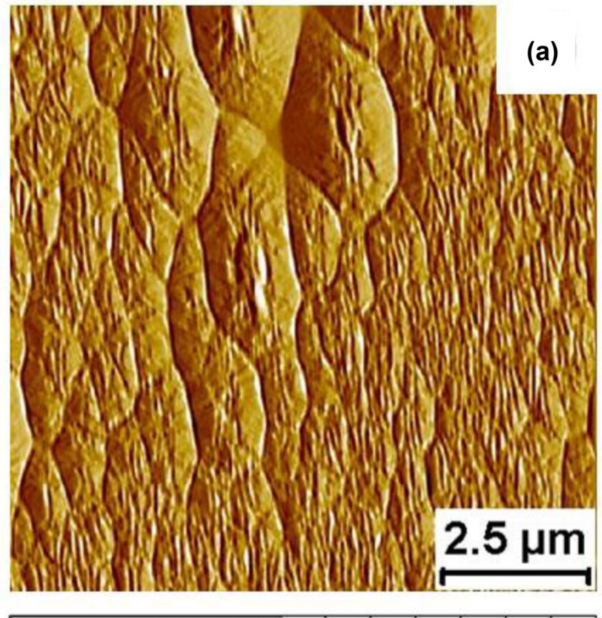

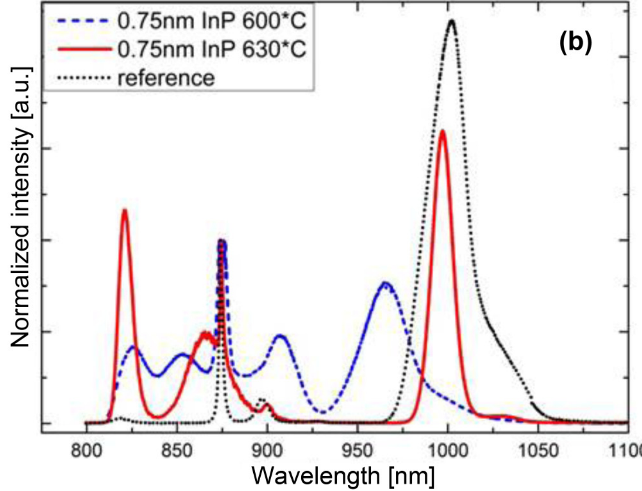

FIG. 10. (a) AFM (signal amplitude) of a representative sample with 0.75 nm InP deposited at 600 °C with AlInAs cladding on p.o. substrate. (b) Low-temperature photoluminescence spectra of samples with 0.75 nm InP deposited at 600 °C (blue dashed line) and 630 °C (red solid line) with reference of bulk AlInAs/InP (black dotted line). The peak pattern in reference sample is typical for the type-II-alignment-induced optical transition of a simple InP-AlInAs interface [51,52].

V. SUMMARY, CONCLUSIONS, AND FUTURE DIRECTIONS

We have shown that the deposition of InP by MOVPE over a broad range of growth conditions on a macroscopically lattice-matched high Al-containing buffer evolves with surprisingly complex morphologies. The expected layer-by-layer growth is perturbed, and often altogether absent, due to a combination of energetic and kinetic factors that favor other types of surface organization. The formation of quantum dots appears to proceed without a wetting layer, being instead consistent with a Volmer-Weber process, and leads to a variety of surfaces morphologies, ranging from dots to rings and their combinations. Each growth parameter change had a

striking influence on the surface organization, demonstrating the intricacies of the interplay between kinetic mechanisms in MOVPE. Indeed, these and similar issues are often overlooked in the community, where an industrial approach is frequently applied to deliver an efficient high-throughput production method. Consequently, the physics behind the complex details of epitaxy in a reactive environment are still poorly understood. Our work goes beyond the importance of controlling surface and interface physics for the specific InP/AlInAs system, and highlights the need for a stronger community focus on a program that combines experiments with the theory and modeling of MOVPE.

To provide a more thorough grasp of one aspect of these complex issues, we analyzed the dependence of the surface morphology on substrate temperature, V/III ratio, and growth rate in terms of characteristic lengths determined by the main kinetic processes in a generalized Burton-Cabrera-Frank model of precursor deposition and decomposition and the subsequent adatom kinetics. This provides a systematic characterization of growth morphology and suggests that a more detailed analysis that involves the numerical integration of the two-dimensional generalized BCF model on misoriented surfaces, as has been done for MBE [53], would prove profitable, in particular for examining the time dependence of the morphology. An analytic alternative based on the solutions of the one-dimensional equations might also yield some semiquantitative insight.

Taking a broader view, epitaxial growth, by whatever means, is an inherently multiscale problem [54]. Here, we have used a top-down analysis based on length scales associated with particular processes of a coarse-grained continuum model. This approach, which replaces the atomistic details of each kinetic process with an effective rate, is eminently suited to long terrace lengths (measured in microns) in MOVPE. The next level of resolution is based on the kinetic Monte Carlo method, which has been used to great effect in modeling MBE, including the effect of precursors in metalorganic MBE [55]. Large terrace lengths are problematic for this method, but hybrid methods have been developed [56] for such applications. At the atomistic level, modern density functional calculations are capable of calculating the rates of processes such as diffusion [57], adatom interactions with the edges of islands [58] and steps [59], and the decomposition of precursors [60]. These methods raise the level of analysis of MOVPE, whether by continuum equations or kinetic Monte Carlo simulations, from semiempirical to first principles.

The importance of our results for the growth of heterostructures and devices should be considered both in terms of detrimental impact, when InP nanostructuring is ignored, and future applications, when intentionally nanostructured epitaxial layers will open possibilities to macroscopically strain-free multilayer device architectures. Indeed, the implementation of non-Al-containing thin layers (i.e., $In_xGa_{1-x}As$, $In_xGa_{1-x}As_yP_{1-y}$), or extreme growth conditions, are required to eliminate the nanostructuring, and we are growing complex, multilayer devices with the unintentional Volmer-Weber InP growth mode under control. The wide range of possible morphologies, however, provides the opportunity for creating targeted devices with tailored nanostructure shapes and distribution, and opens up new application windows when coupled with other quantum objects (e.g., quantum wells), for multicomponent architectures capable, for example, of addressing technological gaps for broad or tunable emitters. A broader understanding of the phenomenology reported here, as well as other open issues (e.g., dopant surfactant effects [30], incorporation vs surfactant for Sb [42] and Bi [61], and consequences on strain and defect management) will strongly benefit the development of fully fledged integrated photonic technology.

One last summary and perspective remark: This work is part of a number of findings we have published in recent years highlighting the dramatic surface effects in III-V epitaxy, and how they influence practically and potentially device physics. These features have been largely underestimated by the MOVPE community. Our paper reinforces in a timely manner the need to understand the complexity of MOVPE growth processes. This is especially relevant as we can anticipate recent findings which highlight more than anything that it is the surface physics that is the source of a number of unresolved issues in MOVPE epitaxy; see, e.g., Ref. [62].

ACKNOWLEDGMENTS

This research was enabled by the Irish Higher Education Authority Program for Research in Third Level Institutions (2007–2011) via the INSPIRE program, by Science Foundation Ireland under Grants No. 10/IN.1/I3000, No. 15/IA/2864, No. 07/SRC/I1173, No. 12/RC/2276, and No. 12/RC/2276-P2, and by EU project FP7-ICT under Grant No. 258033 (MODE-GAP).

APPENDIX: LENGTH SCALES IN PRECURSOR-MEDIATED GROWTH

Our analysis of (1)–(3) is based on identifying length scales determined by particular combinations of the model parameters. This allows for more applicability of our model than does attempting to parametrize the model for a particular set of growth conditions.

Consider first the quantities

$$x_s = \sqrt{D_M \tau}, \quad \ell_\kappa = \sqrt{D_M/\kappa}. \tag{A1}$$

The length x_s is the average distance that a molecule diffuses before desorbing, while ℓ_k is the average distance a molecule diffuses before decomposing to release an adatom. Thus, the first two regimes of importance are distinguished by whether $x_s/\ell_\kappa \gg 1$ or $x_s/\ell_\kappa \ll 1$, i.e., whether the diffusing species are predominantly atoms or molecules. In the first case, we must consider the pertinent length scales associated with the kinetics of adatoms. The quantity $J_{\rm eff} = \kappa n(x)$ is the effective “flux” of adatoms due to the decomposition of molecules. We define the length

$$\ell_A = \sqrt{D_A/J_{\rm eff}}, \tag{A2}$$

where $J_{\rm eff}$ is the constant value obtained by averaging $J_{\rm eff}(x)$ over a terrace. Clearly, ℓ_A corresponds to the distance an adatom diffuses before another adatom is released by a molecular decomposition reaction.

There now are two new regimes to consider: $\ell_A/\ell \ll 1$ and $\ell_A/\ell \gg 1$. In the first case, the typical migration distance of

an adatom is much small than the terrace length, the encounter probability of adatoms is high, and growth proceeds by the nucleation, growth, and coalescence of islands on terraces. In the second case, adatoms diffuse to the step edges before another atom is released, so growth proceeds by the advancement of steps, i.e., step flow.

Within the atomic step flow regime, there are two additional possibilities to consider. We define a length

$$d_A = D_A/\beta_A, \tag{A3}$$

which is the additional distance an atom diffuses (after its first arrival at a step) before incorporation into the solid occurs. If $d_A \ll \ell$, incorporation occurs very soon after the first encounter with a step. We refer to this as "fast atomic step flow." Clearly, $\ell_A \gg \ell \gg d_A$ in this regime. On the other hand, if $d_A \gg \ell$, step-edge incorporation requires several attempts. If $d_A \ll \ell_A$, growth is reaction limited at the step edges of the original surface and occurs by "slow atomic step flow." But, if $d_A \gg \ell_A$, attractive interactions between atoms on the terrace become important and growth occurs by a combination of slow step flow and island formation.

If $x_s/\ell_\kappa \ll 1$, the diffusing species are predominantly the molecular precursors. To determine the growth regimes in this case, we construct the molecular analog to ℓ_A, i.e.,

$$\ell_M = \sqrt{D_M/J}. \tag{A4}$$

The quantity ℓ_M is the average distance a molecule travels before encountering another molecule deposited by the incoming flux. We are thus led to consider the regimes $\ell_M/\ell \ll 1$ and $\ell_M/\ell \gg 1$. In the first case, the molecules diffuse to the step edge before encountering another molecule, while in the second case, the molecules collide on the terraces before arriving at the step edge. Both cases require further consideration.

If $\ell_M/\ell \ll 1$, the encounter probability of the molecules on the terraces is high and several scenarios can occur, depending on the mean density of the precursors. Possibilities include collisional decomposition with concomitant island nucleation, the formation of a molecular film, and the formation of a liquid-like state of adsorbed molecules. Since our model does not include interactions between the molecules, we refer to this simply as the "molecular interaction" regime.

If $\ell_M/\ell \gg 1$, it is useful to determine whether one or several encounters with a step are required before the molecule decomposes. This issue is addressed by introducing the length

$$d_M = D_M/\beta_M, \tag{A5}$$

which may be regarded as the distance a precursor diffuses before a successful step-catalyzed decomposition and incorporation occurs. Again, two regimes are distinguished: $d_M/x_s \ll 1$ and $d_M/x_s \gg 1$. If $d_M/x_s \ll 1$, most of the molecules immediately decompose upon arrival at a step edge. We call this the regime of "fast molecular step flow." Note that $\ell_\kappa \gg x_s \gg d_M$ in this case.

When $d_M/x_s \gg 1$, we must specify the relative magnitudes of d_M and ℓ_κ, since both are much greater than the mean desorption length x_s. If ℓ_κ is the shorter of the two, the molecule decomposes on the terrace and the growth mode is determined by atomic kinetics, as discussed earlier. But, if d_M is the shorter length, the molecules decompose predominantly at the step edge, albeit with some difficulty. We refer to this latter regime as "slow molecular step flow" to indicate that, even though molecular diffusion to the step edge is fast, the subsequent attachment of the adatom is slow.

The hierarchy of regimes is shown in Table II in the main text, with each determined by the relative magnitudes of the various characteristic lengths we have discussed. For each regime we have also provided additional information about the predominant species and kinetics at step edges. Several comments about this table are warranted. The notion of step permeability, first introduced by Ozdemir and Zangwill [63], is a measure of the probability that an atom or molecule crosses the step without being incorporated. Molecular decomposition, which is described by the symmetrical boundary conditions (3), in fact, proceeds at different rates when molecules approach from above or below a step [31,36]. This asymmetry in decomposition rates is responsible for step bunching on misoriented substrates during MOVPE. For the substrates used here, the slow and fast molecular flow conditions become slow and fast transitions to step flow. The A and B steps in Fig. 4 illustrate the differences in these two growth modes.

[1] M. Smit, X. Leijtens, H. Ambrosius, E. Bente, J. van der Tol, B. Smalbrugge, T. de Vries, E. J. Geluk, J. Bolk, R. van Veldhoven, L. Augustin, P. Thijs, D. D'Agostino, H. Rabbani, K. Lawniczuk, S. Stopinski, S. Tahvili, A. Corradi, E. Kleijn, D. Dzibrou, M. Felicetti, E. Bitincka, V. Moskalenko, J. Zhao, R. Santos, G. Gilardi, W. M. Yao, K. Williams, P. Stabile, P. Kuindersma, J. Pello, S. Bhat, Y. Q. Jiao, D. Heiss, G. Roelkens, M. Wale, P. Firth, F. Soares, N. Grote, M. Schell, H. Debregeas, M. Achouche, J. L. Gentner, A. Bakker, T. Korthorst, D. Gallagher, A. Dabbs, A. Melloni, F. Morichetti, D. Melati, A. Wonfor, R. Penty, R. Broeke, B. Musk, and D. Robbins, Semicond. Sci. Technol. **29**, 083001 (2014).

[2] F. Kish, V. Lal, P. Evans, S. W. Corzine, M. Ziari, T. Butrie, M. Reffle, H. S. Tsai, A. Dentai, and J. Pleumeekers, IEEE J. Sel. Top. Quantum Electron. **24**, 1 (2017).

[3] Y. Tian, J. Li, J. D. Kirch, C. Sigler, L. Mawst, E. Pelucchi, F. H. Peters, and D. C. Hall, Phys. Status Solidi A **216**, 1800495 (2019).

[4] S. P. Duggan, H. Yang, N. P. Kelly, L. Caro, M. Dernaika, M. Shayesteh, A. Gocalinska, K. Thomas, E. Pelucchi, B. Corbett, and F. H. Peters, Microwave Opt. Technol. Lett. **60**, 2363 (2018).

[5] E. Lugagne-Delpon, P. Voisin, J. P. Vieren, M. Voos, and J. N. Patillon, Semicond. Sci. Technol. **7**, 524 (1992).

[6] D. Vignaud, X. Wallart, F. Mollot, and B. Sermage, J. Appl. Phys. **84**, 2138 (1998).
[7] L. Aina, M. Mattingly, A. Fathimulla, E. A. Martin, T. Loughran, and L. Stecker, J. Cryst. Growth **93**, 911 (1988).
[8] R. Schwertberger, D. Gold, J. P. Reithmaier, and A. Forchel, IEEE Phot. Tech. Lett. **14**, 735 (2002).
[9] B. L. Sharma, Prog. Cryst. Growth Charact. **12**, 295 (1986).
[10] R. A. D. MacKenzie, J. A. Liddle, C. R. M. Grovenor, and A. Cerezo, J. Phys. Colloq. **50**, C8 (1989).
[11] R. A. Stradling, Phys. Scr. T **T35**, 237 (1991).
[12] See, for example, M. Sacilotti, F. Motisuke, Y. Monteil, P. Abraham, F. Iikawa, C. Montes, M. Furtado, L. Horiuchi, R. Landers, J. Morais, L. Cardoso, J. Decobert, and B. Waldman, J. Cryst. Growth **124**, 589 (1992).
[13] P. Abraham, Y. Monteil, M. Sacilotti, T. Benyattou, M. A. Garcia, S. Moneger, A. Tabata, R. Landers, J. Morais, and M. Pitaval, Appl. Surf. Sci. **65**, 777 (1993).
[14] A. Gocalinska, M. Manganaro, G. Juska, V. Dimastrodonato, K. Thomas, B. A. Joyce, J. Zhang, D. D. Vvedensky, and E. Pelucchi, Appl. Phys. Lett. **104**, 141606 (2014).
[15] F. C. Frank and J. H. van der Merwe, Proc. R. Soc. London, Ser. A **198**, 205 (1949).
[16] E. Bauer, Z. Kristallogr. **110**, 372 (1958).
[17] R. Kern, G. Le Lay, and J. J. Métois, Curr. Top. Mater. Sci. **3**, 131 (1979).
[18] M. Volmer and A. Weber, Z. Phys. Chem. **119**, 277 (1926).
[19] S. Raghavan and J. M. Redwing, J. Appl. Phys. **96**, 2995 (2004).
[20] B. Moran, F. Wu, A. E. Romanov, U. K. Mishra, S. P. Denbaars, and J. S. Speck, J. Cryst. Growth **273**, 38 (2004).
[21] Ch. Meissner, S. Ploch, M. Pristovsek, and M. Kneissl, Phys. Status Solidi C **6**, S545 (2009).
[22] M. C. Harris Liao, Y. H. Chang, Y. F. Chen, J. W. Hsu, J. M. Lin, and W. C. Chou, Appl. Phys. Lett. **70**, 2256 (1997).
[23] H. Li and B. P. Tonner, Surf. Sci. **237**, 141 (1990).
[24] E. Navas, P. Schuster, C. M. Schneider, J. Kirschner, A. Cebollada, C. Ocal, R. Miranda, J. Cerdá, and P. de Andrés, J. Magn. Magn. Mater. **121**, 65 (1993).
[25] J. Fassbender, R. Allenspach, and U. Dürig, Surf. Sci. **383**, L742 (1997).
[26] D. D. Vvedensky and S. Clarke, MRS Symp. Proc. **160**, 221 (1989).
[27] S. V. Kolesnikov, A. L. Klavsyuk, and A. M. Saletsky, Phys. Solid State **51**, 1254 (2009).
[28] E. Mura, A. Gocalinska, G. Juska, S. T. Moroni, A. Pescaglini, and E. Pelucchi, Appl. Phys. Lett. **110**, 113101 (2017).
[29] See Supplemental Material at http://link.aps.org/supplemental/10.1103/PhysRevB.101.165310 for additional line scans and images.
[30] A. Gocalinska, M. Manganaro, E. Pelucchi, and D. D. Vvedensky, Phys. Rev. B **86**, 165307 (2012).
[31] A. L. S. Chua, E. Pelucchi, A. Rudra, B. Dwir, E. Kapon, A. Zangwill, and D. D. Vvedensky, Appl. Phys. Lett. **92**, 013117 (2008).
[32] E. Pelucchi, N. Moret, B. Dwir, D. Y. Oberli, A. Rudra, N. Gogneau, A. Kumar, E. Kapon, E. Levy, and A. Palevski, J. Appl. Phys. **99**, 093515 (2006).
[33] V. Dimastrodonato, L. O. Mereni, R. J. Young, and E. Pelucchi, J. Cryst. Growth **312**, 3057 (2010).
[34] W. K. Burton, N. Cabrera, and F. C. Frank, Philos. Trans. R. Soc. London, Sec. A **243**, 299 (1951).
[35] R. Ghez and S. S. Iyer, IBM J. Res. Dev. **32**, 804 (1988).
[36] A. Pimpinelli and A. Videcoq, Surf. Sci. **445**, L23 (2000).
[37] V. Dimastrodonato, E. Pelucchi, and D. D. Vvedensky, Phys. Rev. Lett. **108**, 256102 (2012).
[38] V. Dimastrodonato, E. Pelucchi, P. A. Zestanakis, and D. D. Vvedensky, Phys. Rev. B **87**, 205422 (2013).
[39] S. T. Moroni, V. Dimastrodonato, T.-H. Chung, G. Juska, A. Gocalinska, D. D. Vvedensky, and E. Pelucchi, J. Appl. Phys. **117**, 164313 (2015).
[40] L. J. Brillson, *An Essential Guide to Electronic Materials Surfaces and Interfaces* (Wiley, Chichester, UK, 2016).
[41] Note that two-dimensional AFM images are always computed figures with subsequent scanned lines aligned by the software. Normally, the Y "line" is less reliable in an X scanned image, and good practice dictates not to use this image to extract physical information about relative height. However, in this case, we have performed corresponding measurements in both scanning directions to confirm the values and we are confident that the given numbers are correct. Therefore, we show a single image with both X and Y profiles, not to duplicate the information.
[42] A. Gocalinska, M. Manganaro, and E. Pelucchi, Appl. Phys. Lett. **100**, 152112 (2012).
[43] T. Shitara, D. D. Vvedensky, M. R. Wilby, J. Zhang, J. H. Neave, and B. A. Joyce, Phys. Rev. B **46**, 6825 (1992).
[44] J. W. Evans, P. A. Thiel, and M. C. Bartelt, Surf. Sci. Rep. **61**, 1 (2006).
[45] Y. A. Kryukov and J. G. Amar, Phys. Rev. B **81**, 165435 (2010).
[46] J. A. Venables, G. D. T. Spiller, and M. Hanbücken, Rep. Prog. Phys. **47**, 399 (1984).
[47] D. V. Lebedev, M. M. Kulagina, S. I. Troshkov, A. S. Vlasov, V. Y. Davydov, A. N. Smirnov, A. A. Bogdanov, J. L. Merz, J. Kapaldo, A. Gocalinska, G. Juska, S. T. Moroni, E. Pelucchi, D. Barettin, S. Rouvimov, and A. M. Mintairov, Appl. Phys. Lett. **110**, 121101 (2017).
[48] J. Sormunen, J. Riikonen, M. Mattila, J. Tiilikainen, M. Sopanen, and H. Lipsanen, Nano Lett. **5**, 1541 (2005).
[49] Z. Y. Zhou, C. X. Zheng, W. X. Tang, J. Tersoff, and D. E. Jesson, Phys. Rev. Lett. **111**, 036102 (2013).
[50] T. P. Schulze and P. Smereka, Phys. Rev. B **86**, 235313 (2012).
[51] P. Abraham, M. A. Garcia Perez, T. Benyattou, G. Guilloti, F. Sacilotti, and X. Letartre, Semicond. Sci. Technol. **10**, 1585 (1995).
[52] W. Seidel, A. Titkov, J. P. André, P. Voisin, and M. Voos, Phys. Rev. Lett. **73**, 2356 (1994).
[53] A. K. Myers-Beaghton and D. D. Vvedensky, Phys. Rev. A **44**, 2457 (1991).
[54] D. D. Vvedensky, J. Phys.: Condens. Matter **16**, R1537(R) (2004).
[55] T. Shitara, T. Kaneko, and D. D. Vvedensky, Appl. Phys. Lett. **63**, 3321 (1993).
[56] G. Russo, L. M. Sander, and P. Smereka, Phys. Rev. B **69**, 121406(R) (2004).
[57] M. Rosini, P. Kratzer, and R. Magri, J. Phys.: Condens. Matter **21**, 355007 (2009).
[58] P. Kratzer, E. Penev, and M. Scheffler, Appl. Phys. A **75**, 79 (2002).
[59] P. Kratzer, C. G. Morgan, and M. Scheffler, Prog. Surf. Sci. **59**, 135 (1998).

[60] H. Tetlow, J. Posthuma de Boer, I. J. Ford, D. D. Vvedensky, D. Curcio, L. Omiciuolo, S. Lizzit, A. Baraldi, and L. Kantorovich, Phys. Chem. Chem. Phys. **18**, 27897 (2016).

[61] T. Matsuda, K. Takada, K. Yano, R. Tsutsumi, K. Yoshikawa, S. Shimomura, Y. Shimizu, K. Nagashima, T. Yanagida, and F. Ishikawa, Nano Lett. **19**, 8510 (2019).

[62] A. Ozcan-Atar, A. Gocalinska, P. P. Michalowski, and E. Pelucchi, Oral presentation: An unusual dopant profile of InP during metal organic vapor phase epitaxy, Compound Semiconductor Week 2020, 17–21 May, Stockholm.

[63] M. Ozdemir and A. Zangwill, Phys. Rev. B **45**, 3718 (1992).